Modeling Low-G Slosh Using Negative Mass

Matthew M. Wittal*, William Dziedzic†, and Jonathan S. Pitt ‡
NASA Deep Space Logistics Project Office, Kennedy Space Center FL, 32899

Brennan McCann§, Marco Fagetti¶, and Morad Nazari‖
Embry-Riddle Aeronautical University, 1 Aerospace Blvd., FL, 32114

The modeling of the behavior of fluids in low- or microgravity is a field with little validated data but of great interest to space agencies and companies in the face of humanity's expanding presence beyond low Earth orbit. Efforts to refuel and repair satellites in geostationary orbit require an understanding of the behavior of sloshing fuel in microgravity. The stability of remote sensing equipment and satellites depends on robust fluid slosh dampening or very accurate modeling, and the Artemis program includes the refueling of large landing systems in its architecture. However, current methodologies are quite binary: either use a relatively low-accuracy equivalent mechanical model or use computational fluid dynamics which are not practical for onboard systems due to their relatively high computational cost. In this work, a novel method of tracking the bubble rather than tracking the fuel itself is presented. Computational fluid dynamics simulations are used to validate the model based on available experimental data, and the dynamics of a refueler spacecraft based on Gateway's Logistics Module are simulated both for the sloshing case and without sloshing considered.

I. Introduction

Increasing the fidelity of state and parameter estimation is a necessary component in the development of robust autonomy for deep space exploration, as well as for autonomy's fault detection on manned systems. Having models that are both robust and easy to compute is critical when considering the limitations of onboard computational resources. There are many components to a dynamical model, and depending on the spacecraft system in question, some of the dynamics may be ignored for simplicity, while in other cases they may play a dominant role in the dynamics of the spacecraft. Oscillating solar panels may play a major role in the attitude dynamics of a probe, such as Juno [1], where the solar panels are significantly longer than the spacecraft itself, yet be negligible in smaller spacecraft with solar panels mounted close to the fuselage of the spacecraft, such as Hubble. In this work, refueling spacecraft and spacecraft with very large fuel tanks are of specific interest, and in these systems, slosh dynamics play a far more significant role than in legacy spacecraft with much more humble fuel reserves.

Slosh dynamics in low- and microgravity (and indeed, slosh dynamics in general) present a unique problem for spacecraft attitude dynamics and control. Historically, simple approximations such as the pendulum and spring-mass-damper models have been used to model the behavior of fluids in launch vehicles and have been adequate in terrestrial and high-g environments. For spacecraft, other models have been developed that approximate the motion of sloshing fluids in microgravity, such as the moving pulsating ball model [2]. Finally, computational fluid dynamics (CFD) provide high-fidelity simulations that are thought to approximate the motion of fluids in microgravity with a high level of detail [3–5], though with very little on-orbit experimental data to validate these models, their accuracy has yet to be confirmed.

However, with increasing complexity comes increasing computational cost and, thus, increased power and mass demands for on-board space systems. CFD simulations are beginning to process 1 second of real-time motion in 1 second of computation time on multicore high-end platforms, yet this remains impractical for space applications. Simple models for onboard dynamical models in spacecraft are still needed. The existing equivalent mechanical models,

*Automation and Robotics Systems Engineer / Ph.D. Candidate, Deep Space Logistics, NASA Kennedy Space Center, AIAA Student Member / Aerospace Engineering Department, Embry-Riddle Aeronautical University

†Gas and Fluid Systems Engineer, NASA Kennedy Space Center

‡SME, Computational Fluid Dynamics, Aegis Aerospace, Kennedy Space Center, FL, 32899

§Ph.D. Candidate, Aerospace Engineering Department, Embry-Riddle Aeronautical University

¶Ph.D. Student, Aerospace Engineering Department, Embry-Riddle Aeronautical University

‖Assistant Professor, Aerospace Engineering Department, Embry-Riddle Aeronautical University, AIAA Senior Member

namely the spring-mass-damper and pendulum models, are computationally efficient but do not accurately approximate what little we know of microgravity slosh. This work proposes a more accurate version of the spring-mass-damper model with a negligible increase in computational load. By tracking the air bubble, or "negative mass", instead of the fluid itself, it is possible to approximate the center of mass and moments of inertia of a sloshing fluid with reasonable accuracy, while not increasing computational load.

In this paper, preliminaries of the special Euclidian group $\mathsf{SE}(3)$ are described in Section II as the foundation of the spacecraft dynamics considered. This is followed by a description of slosh dynamics using the negative mass model (NMM). In Section III, the case studies considered in this work are introduced and simulated using the Star-CCM+ CFD software. Then, the NMM simulations are shown for the same case studies in Section IV. The relative performance of these models is discussed in Section V, and conclusions and future work are then stated in Section VI.

II. Preliminaries

Spacecraft dynamics in this work are modeled in the $\mathsf{SE}(3)$ rigid body framework, and the dynamics of the bubble are modeled geometrically. The following sections describe these formulations separately, and then together as a transfer of momentum between body and tank.

A. Dynamics on Special Euclidean Group $\mathsf{SE}(3)$

The pose of a rigid body is expressed in $\mathsf{SE}(3)$ as

$$g = \begin{bmatrix} R & r \\ 0_{1\times 3} & 1 \end{bmatrix} \in \mathsf{SE}(3) \tag{1}$$

where $R \in \mathsf{SO}(3)$ is the attitude expressed as a rotation matrix and r is the position vector in the inertial frame. Note that the rotation matrix rotates from a rigid body frame $\mathcal{B}$ to some inertial frame $\mathcal{N}$. The rigid body's velocity can be defined using an augmented velocity vector $\mathbb{V}$ as

$$\mathbb{V} = \left[\omega^T, v^T\right]^T \in \mathbb{R}^6 \tag{2}$$

such that $\omega \in \mathbb{R}^3$ is the angular velocity in the body frame $\mathcal{B}$ and $v \in \mathbb{R}^3$ is the translational velocity relative to the inertial frame and expressed in the body frame. For the purpose of developing a formulation for relative motion or tracking controller on $\mathsf{SE}(3)$, the following expression is introduced:

$$\epsilon_g = g_d^{-1} g = \begin{bmatrix} \epsilon_R & \epsilon_r \\ 0 & 1 \end{bmatrix} = \begin{bmatrix} R_d^T R & R_d^T (r - r_d) \\ 0 & 1 \end{bmatrix} \in \mathsf{SE}(3) \tag{3}$$
$$\epsilon_{\mathbb{V}} = \mathbb{V} - \mathrm{Ad}_{\epsilon_g^{-1}} \mathbb{V}_d \in \mathbb{R}^6$$

where the subscript d denotes the desired or modeled state or parameter. The relative dynamics of a rigid body with a changing center of mass and moments of inertia in $\mathsf{SE}(3)$ are represented in the dynamic model as

$$\dot{\epsilon}_g = \epsilon_g \epsilon_{\mathbb{V}}^{\vee} \in \mathfrak{se}(3) \tag{4a}$$

$$\dot{\epsilon}_{\mathbb{V}} = \mathbb{I}^{-1} \left(\mathrm{ad}^*_{\epsilon_{\mathbb{V}}} \mathbb{I} \epsilon_{\mathbb{V}} + \tau + u\right) \in \mathbb{R}^6 \tag{4b}$$

where

$$\mathbb{I} = \begin{bmatrix} J & 0_{3\times 3} \\ 0_{3\times 3} & mI_3 \end{bmatrix} \in \mathbb{R}^{6\times 6}, \tag{5}$$

The co-adjoint operator is defined as

$$\mathrm{ad}^*_{\mathbb{V}} = \mathrm{ad}^T_{\mathbb{V}} = \begin{bmatrix} -\omega^\times & -v^\times \\ 0_{3\times 3} & -\omega^\times \end{bmatrix} \in \mathbb{R}^{6\times 6} \tag{6}$$

where the adjoint operator $\mathrm{ad}_{\mathbb{V}}$ is

$$\mathrm{ad}_{\mathbb{V}} = \begin{bmatrix} \omega^\times & 0_{3\times 3} \\ v^\times & \omega^\times \end{bmatrix} \in \mathbb{R}^{6\times 6} \tag{7}$$

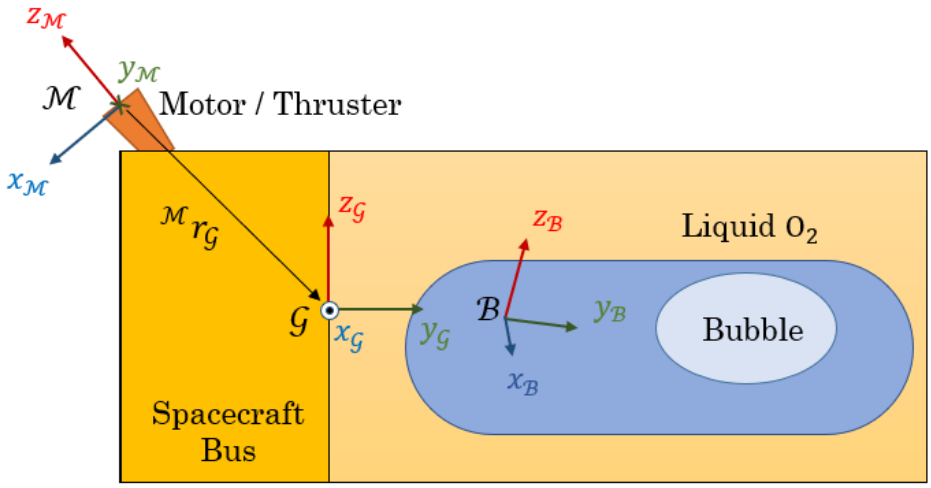

Fig. 1 An illustration of the different reference frames and notations.

In Eq. (4), $\tau \in \mathbb{R}^6$ represents the impressed dynamics acting on the system expressed in the $\mathcal{B}$ frame. Furthermore, the augmented vector of control inputs is given by $u = \left[L^T, f^T\right]^T \in \mathbb{R}^6$ where $f \in \mathbb{R}^3$ and $L \in \mathbb{R}^3$ represent the control forces and torques, respectively.

A geometric frame $\mathcal{G}$ is defined as a fixed point on the vehicle. The geometric frame is defined relative to the body frame as

$$g_{\mathcal{G}} = \begin{bmatrix} {}^{\mathcal{G}}R_{\mathcal{B}} & r_{\mathcal{G}} \\ 0_{1\times 3} & 1 \end{bmatrix} \in \mathsf{SE}(3) \tag{8}$$

Similarly, consider an actuator $g_{\mathcal{M}} \in \mathsf{SE}(3)$ where $\mathcal{M}$ denotes the frame of the actuator with respect to the rigid body which has a pose defined as

$$g_{\mathcal{M}} = \begin{bmatrix} {}^{\mathcal{M}}R_{\mathcal{B}} & r_{\mathcal{M}} \\ 0_{1\times 3} & 1 \end{bmatrix} \in \mathsf{SE}(3) \tag{9}$$

where ${}^{\mathcal{M}}R_{\mathcal{M}}$ is the attitude of the thruster in the body frame $\mathcal{M}$, and $r_{\mathcal{M}}$ is the position of the geometric reference point with respect to the thruster. The relative motion dynamics expressed above may be extended to describe the pose of a thruster relative to a central body. This may be expressed as $g_{\mathcal{M}}$. Take the linear adjoint operator of this relative configuration to yield

$$\mathrm{Ad}_{g_{\mathcal{M}/\mathcal{B}}} = \begin{bmatrix} {}^{\mathcal{M}}R_{\mathcal{B}} & 0_{3\times 3} \\ r_{\mathcal{M}}^{\times}\,{}^{\mathcal{M}}R_{\mathcal{B}} & {}^{\mathcal{M}}R_{\mathcal{B}} \end{bmatrix} \in \mathbb{R}^{6\times 6} \tag{10}$$

The transpose of the adjoint operator is defined as

$$\mathrm{Ad}^T_{g_{\mathcal{M}/\mathcal{B}}} = \begin{bmatrix} {}^{\mathcal{M}}R_{\mathcal{B}}^T & -{}^{\mathcal{M}}R_{\mathcal{B}}^T r_{\mathcal{M}}^{\times} \\ 0_{3\times 3} & {}^{\mathcal{M}}R_{\mathcal{B}}^T \end{bmatrix} \in \mathbb{R}^{6\times 6} \tag{11}$$

And finally,

$$\mathrm{Ad}^T_{g^{-1}_{\mathcal{M}/\mathcal{B}}} = \begin{bmatrix} {}^{\mathcal{M}}R_{\mathcal{B}} & {}^{\mathcal{M}}R_{\mathcal{B}}\left({}^{\mathcal{M}}R_{\mathcal{B}}^T r_{\mathcal{M}}\right)^{\times} \\ 0_{3\times 3} & {}^{\mathcal{M}}R_{\mathcal{B}} \end{bmatrix} \in \mathbb{R}^{6\times 6} \tag{12}$$

However, an intermediate frame $\mathcal{G}$ may be defined to represent the geometric frame, defined at some fixed point on the rigid body $r_{\mathcal{G}}$ relative to the body frame $\mathcal{B}$ about the center of mass.

$$\mathrm{Ad}^T_{g^{-1}_{\mathcal{M}/\mathcal{B}}} = \begin{bmatrix} {}^{\mathcal{M}}R_{\mathcal{B}} & {}^{\mathcal{M}}R_{\mathcal{B}}\left({}^{\mathcal{M}}R^T_{\mathcal{B}} r_{\mathcal{M}}\right)^{\times} \\ 0_{3\times 3} & {}^{\mathcal{M}}R_{\mathcal{B}} \end{bmatrix} = \begin{bmatrix} {}^{\mathcal{M}}R_{\mathcal{B}} & {}^{\mathcal{M}}R_{\mathcal{B}}\left(\left({}^{\mathcal{M}}R^T_{\mathcal{G}} r_{\mathcal{M}}\right)^{\times} + \left({}^{\mathcal{G}}R^T_{\mathcal{B}} r_{\mathcal{G}}\right)^{\times}\right) \\ 0_{3\times 3} & {}^{\mathcal{M}}R_{\mathcal{B}} \end{bmatrix}$$

$$= \begin{bmatrix} {}^{\mathcal{G}}R_{\mathcal{B}} & {}^{\mathcal{G}}R_{\mathcal{B}}\left({}^{\mathcal{G}}R^T_{\mathcal{B}} r_{\mathcal{G}}\right)^{\times} \\ 0_{3\times 3} & {}^{\mathcal{G}}R_{\mathcal{B}} \end{bmatrix} \begin{bmatrix} {}^{\mathcal{M}}R_{\mathcal{G}} & {}^{\mathcal{M}}R_{\mathcal{G}}\left({}^{\mathcal{M}}R^T_{\mathcal{G}} r_{\mathcal{M}}\right)^{\times} \\ 0_{3\times 3} & {}^{\mathcal{M}}R_{\mathcal{G}} \end{bmatrix} = \mathrm{Ad}^T_{g^{-1}_{\mathcal{G}/\mathcal{B}}} \mathrm{Ad}^T_{g^{-1}_{\mathcal{M}/\mathcal{G}}} \tag{13}$$

A spacecraft configuration with static RCS thrusters located on the spacecraft bus relative to the spacecraft geometric frame $\mathcal{G}$ and the body frame $\mathcal{B}$, subject to sloshing fluid, is illustrated in Figure 1. As described in detail in [6], homogeneous distribution of total thrust capacity may be assumed such that $u = \sum_{n=1}^{N} u_n \in \mathbb{R}^6$, where u_n is the control input on the n^{th} actuator and N is the total number of actuators. The motor frames are expressed as $T_{\mathcal{M},n} = [0, 0, 0, 0, 0, -F_n(t)]^T \in \mathbb{R}^6$, where $F_n(t) \in \mathbb{R}$ is the force from thruster n at time t. Equation 13 is used such that an arbitrary actuator or motor can be modeled in reference to either a geometric or body frame coordinate system. In this work, the geometric center of the tank is described relative to an arbitrary motor frame. As such, it can be seen that $\mathrm{Ad}_{g^{-1}_{\mathcal{M}}} T_{\mathcal{M},n} \in \mathbb{R}^6$ can fully compute the torques and forces acting on the rigid body from the control inputs centered at the n^{th} actuator in N, where N is the full set of actuations. As a result, the final control input acting on the rigid body from the n^{th} actuator can be given as

$$u_n = \mathrm{Ad}^T_{g^{-1}_{\mathcal{M},n}} T_{\mathcal{M},n} \in \mathbb{R}^6 \tag{14}$$

This expression is convenient because the control inputs in the $\mathcal{M}$ frame should be known based on actuator specifications, and the actuator's configuration relative to the rigid body should also be known based on the rigid body's design parameters.

B. Bubble Deformation Dynamics

The dynamical model for the geometric shape of the model is determined by three key properties: a dampening coefficient, which is related to the viscosity of the fluid; a surface tension coefficient, which is experimentally derived;

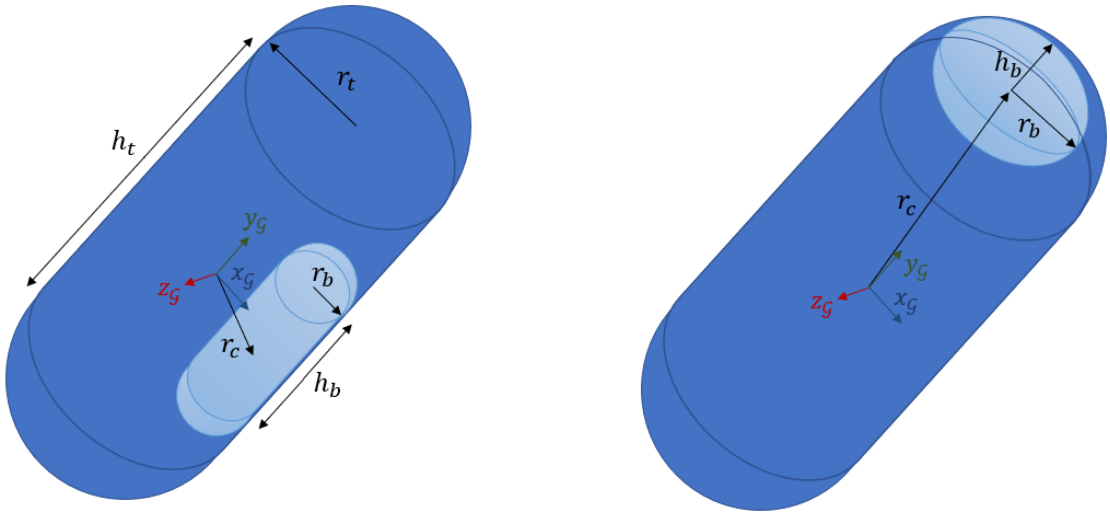

a. Capsule deformation impact

b. Ellipsoid deformation impact

Fig. 2 An illustration of the terminology used in Algorithm 1 (a) and 2, (b)

Algorithm 1 Capsule Bubble Deformation Against a Flat Surface in the x-direction

if $r_{c,x}(t_{k+1}) + r_b(t_0) > r_t$ **then**
  $r_{b,x}(t_{k+1}) = r_t - r_{c,x}(t_{k+1})$
  $h_b(t_{k+1}) = \frac{V_b}{\pi r_b^2(t_{k+1})} - \frac{4}{3} r_b(t_{k+1})$
  if $h_b(t_{k+1}) > h_t$ **then**
    $h_b(t_{k+1}) = h_t$
    $\dot{r}_{c,x} = \dot{r}_{c,x} - \ddot{r}_{c,x} dt$
    $r_b(t_{k+1}) = \text{Re}\left(\text{roots}([\frac{4}{3}, h_t, 0, -\frac{V_b}{\pi}])\right)$
  else if $\frac{h_b(t_{k+1})}{2} - r_{b,y}(t_{k+1}) > \frac{h_t}{2}$ **then**
    $h_b(t_{k+1}) = h_t + 2r_{b,x}(t_{k+1})$
    $\dot{r}_y = \dot{r}_{c,y} - \ddot{r}_{c,y} dt$
  else if $-\frac{h_b(t_{k+1})}{2 - r_{b,y}(t_{k+1})} < -\frac{h_t}{2}$ **then**
    $h_b(t_{k+1}) = h_t + 2r_{b,x}(t_{k+1})$
    $\dot{r}_{c,y} = \dot{r}_{c,y} - \ddot{r}_{c,y} dt$
  end if
else if $r_{c,x}(t_{k+1}) - r_b(t_0) > -r_t$ **then**
  $r_{b,x}(t_{k+1}) = r_t + r_{c,x}(t_{k+1})$
  $h_b(t_{k+1}) = \frac{V_b}{\pi r_b^2(t_{k+1})} - \frac{4}{3} r_b(t_{k+1})$
  if $h_b(t_{k+1}) > h_t$ **then**
    $h_b(t_{k+1}) = h_t$
    $\dot{r}_{c,x} = \dot{r}_{c,x} - \ddot{r}_{c,x} dt$
    $r_b(t_{k+1}) = \text{Re}\left(\text{roots}([\frac{4}{3}, h_t, 0, -\frac{V_b}{\pi}])\right)$
  else if $\frac{h_b(t_{k+1})}{2} - r_{b,y}(t_{k+1}) > \frac{h_t}{2}$ **then**
    $h_b(t_{k+1}) = h_t + 2r_{b,x}(t_{k+1})$
    $\dot{r}_y = \dot{r}_{c,y} - \ddot{r}_{c,y} dt$
  else if $-\frac{h_b(t_{k+1})}{2 - r_{b,y}(t_{k+1})} < -\frac{h_t}{2}$ **then**
    $h_b(t_{k+1}) = h_t + 2r_{b,x}(t_{k+1})$
    $\dot{r}_{c,y} = \dot{r}_{c,y} - \ddot{r}_{c,y} dt$
  end if
end if
Note: $\epsilon \in \mathbb{R} << 1$, usually $1e^{-5}$

and the geometric boundary of the tank. The shape of the bubble is determined based on the surface with which it collides. For a flat surface, the bubble deforms in a capsule shape, while collisions with a hemisphere are modeled as deformations into an oblate spheroid. The deformation is a function of time and velocity. This is essentially an augmented spring-mass-damper system with conditional statements for tank geometry and angular motion. The acceleration acting on the bubble in the tank, $\ddot{r}_c$, is the negative of the acceleration of the fluid and may be expressed as

$$\ddot{\mathbf{r}}_c = \frac{d^2\mathbf{r}}{dt^2} + \omega \times (\omega \times \mathbf{r}) + 2\omega \times \dot{\mathbf{r}}_c + \dot{\omega} \times \mathbf{r} \tag{15}$$

where

$$\frac{d^2 r}{dt^2} = \frac{\gamma}{m}\dot{\mathbf{r}}_c - \frac{k}{m}\mathbf{r}_c \tag{16}$$

The units for dampening coefficient γ are $\frac{\text{kg}}{\text{s}}$, which is related to the viscosity of the fluid. μ, which has units of $\frac{\text{kg}}{\text{s}\cdot\text{m}}$ by $\gamma = \mu c$ is the surface tension coefficient and acts like the spring part of the system, where c is the cross-sectional circumference of the bubble for each given axis in meters. The surface tension coefficient, k, has units of $\frac{\text{kg}}{s^2}$, or $\frac{\text{N}}{\text{m}}$. Here, m is the mass of the fluid, calculated by subtracting the volume of the bubble from the volume of the tank and multiplying it by the density of the fluid, ρ.

The dynamics above are used to calculate the updated velocity and apply indefinitely for a tank of infinite size. However, for a tank with finite dimensions, boundary conditions must be applied. Two types of collisions are considered

Algorithm 2 Oblate Bubble Deformation Against a Hemisphere in the y-direction

VAL=max$\left([r_b(t_0), r_b(t_{k+1}) + \frac{h_b(t_{k+1})}{2}]\right)$
if $r_{c,y}(t_{k+1})$+VAL$> h_t + \sqrt{r_t^2 - r_{c,x}^2} + \epsilon$ **then**
  $r_b(t_{k+1}) = \frac{h_t}{2} + r_t - r_{c,y}(t_{k+1})$
  $h_b(t_{k+1}) = \sqrt{\frac{3V_b}{4\pi r_b(t_{k+1})}}$
  if $h_b(t_{k+1}) > \sqrt{r_t^2 - (r_t - r_b(t_{k+1}))^2}$ **then**
    $h_b(t_{k+1}) = \sqrt{r_t^2 - (r_t - r_b(t_{k+1}))^2}$
    $\dot{r}_{c,y} = \dot{r}_{c,y} - \ddot{r}_{c,y}dt$
    $r_b(t_{k+1}) = \frac{3V_b}{4\pi r_b(t_{k+1})}$
  end if
  $r_{c,y} = \frac{h_t}{2} + r_t - r_b(t_{k+1})$
else if $r_{c,y}(t_{k+1})$−VAL$< -h_t - \sqrt{r_t^2 - r_{c,x}^2} - \epsilon$ **then**
  $r_b(t_{k+1}) = \frac{h_t}{2} + r_t + r_{c,y}(t_{k+1})$
  $h_b(t_{k+1}) = \sqrt{\frac{3V_b}{4\pi r_b(t_{k+1})}}$
  if $h_b(t_{k+1}) > \sqrt{r_t^2 - (r_t - r_b(t_{k+1}))^2}$ **then**
    $h_b(t_{k+1}) = \sqrt{r_t^2 - (r_t - r_b(t_{k+1}))^2}$
    $\dot{r}_{c,y} = \dot{r}_{c,y} - \ddot{r}_{c,y}dt$
    $r_b(t_{k+1}) = \frac{3V_b}{4\pi r_b(t_{k+1})}$
  end if
  $r_{c,y} = -\frac{h_t}{2} - r_t + r_b(t_{k+1})$
end if
Note: $\epsilon \in \mathbb{R} << 1$, usually $1e^{-5}$

based on the location of the impact: capsule deformation and ellipsoid deformation. Both collisions refer to a deformation in the bubble that maintains a constant volume defined by the initial, spherical shape of the bubble with radius r_o. For an impact with a flat surface, the bubble deforms in a roughly capsule-like shape with the degree of deformation at time step t_{k+1} determined by the magnitude of velocity at time step t_k, detailed in Algorithm 1, and illustrated in Figure 2.a. In the case of an impact with a hemisphere, the dimensions of the bubble can be roughly approximated by an oblate spheroid with bounds and oblateness constrained by the curvature of the hemisphere itself, as described in Algorithm 2

In the case of a capsule-shaped fuel tank used in the remainder of this work, the deformation of the bubble is defined as a capsule deformation about the x-axis but as an oblate spheroid deformation about the y- and z-axes. The variables r_c, $\dot{r}_c$, and $\ddot{r}_c$ are the position of the centroid of the bubble and its time derivatives for velocity and acceleration. The value ϵ is a small error tolerance to differentiate between a bubble the same size as the tank and a bubble colliding with the tank, in this case 1×10^{-5}. Finally, V_b is the volume of the bubble and, considering that the fluid is treated as incompressible, is a constant value.

III. High-Fidelity Simulations

Computational Fluid Dynamics (CFD) simulations of the tank sloshing scenario serve as a comparison and benchmark for the performance and accuracy of the negative mass model presented in this work. While the CFD models are expected to capture more detailed and complex multiphase fluid dynamics phenomena, overall prediction trends between the negative mass and CFD models are expected to be similar.

A Volume-of-Fluid (VOF) two-phase fluid model is chosen to represent the tank sloshing scenario, with a single liquid oxygen phase (LOx) and single helium gas phase (He) that are immiscible, do not have any phase interactions beyond surface tension, and have a non-slip interface. Due to the slow dynamics of the system, the flow is treated as laminar with no sub-grid turbulence modeling. The system is also assumed to be isothermal, and the two fluids are assumed to have constant density and dynamic viscosity, (ρ_{He},ρ_{LOx}) and (μ_{He},μ_{LOx}), respectively, given in Table 1.

	Mass Density (ρ)	Dynamic Viscosity (μ)
Liquid Oxygen (LOx)	1190.6 kg/m^3	2.6139E-4 Pa · s
Helium Gas (He)	0.6087 kg/m^3	8.5034E-6 Pa · s

Table 1 Material properties for the fluids in the CFD simulation. Values are for a pressure of $p = 1$ Pa and a temperature of $T = 80$ K, and were obtained from the NIST database [7].

Define a volume phase fraction field $0 \leq \alpha(x,t) \leq 1$ where $\alpha = 0$ denotes a point that is purely helium and $\alpha = 1$ denotes a point that is purely liquid oxygen. Further defining the velocity ($\mathbf{u}$), total pressure (p), applied volumetric acceleration ($\mathbf{b}$), and the surface tension force ($\mathbf{f}_\sigma$), the equations of motion for the system are given by

$$\frac{\partial(\rho\mathbf{u})}{\partial t} + \nabla\cdot(\rho\mathbf{u}\otimes\mathbf{u}) - \nabla\cdot(\mu\mathbf{D}) = -\nabla p + \rho\mathbf{b} + \rho\mathbf{f}_\sigma, \tag{17}$$

$$\nabla\cdot\mathbf{u} = 0, \tag{18}$$

$$\frac{\partial\alpha}{\partial t} + \nabla\cdot(\alpha\mathbf{u}) = 0, \tag{19}$$

where $\mathbf{D} = \frac{1}{2}\left(\nabla\mathbf{u} + \nabla\mathbf{u}^T\right)$ is the symmetric velocity gradient, and the weighted density and dynamic viscosity are defined as $\rho = \alpha\rho_{Lox} + (1-\alpha)\rho_{He}$ and $\mu = \alpha\mu_{Lox} + (1-\alpha)\mu_{He}$, respectively. Equations (17–19) are solved by the collection of the velocity, pressure, and volume phase fraction fields $(\mathbf{u}, p, \alpha)$ throughout the domain at any time during the simulations.

The surface tension is modeled following the approach of Brackbill et al. [8], and the surface tension force is defined on the fluid-gas interface surface as

$$\mathbf{f}_\sigma = \sigma\kappa\mathbf{n} = -\sigma\nabla\cdot\left(\frac{\nabla\alpha}{|\nabla\alpha|}\right)\nabla\alpha. \tag{20}$$

Here both the surface curvature (κ) of the fluid-gas interface and its normal vector ($\mathbf{n}$) are computed from the volume fraction field. Note that where the volume fraction field is constant, away from the interface, this term is zero. The surface tension constant value in these simulations is $\sigma = 0.0132$ N m^{-1} and was determined empiracally in [9].

The physical model is implemented via the CFD software package Star-CCM+. Third-order spatial discretization via a Monotonic Upwind-centered Scheme for Conservation Laws (MUSCL) scheme is selected, as is a second-order accurate time-stepping scheme. The overall algorithm is a standard single-step segregated SIMPLE style algorithm with five inner correctors per time-step to ensure residual convergence. The well-known second-order high-resolution interface capturing (HRIC) scheme is selected for interface sharpening, with a sharpening factor set to one-half, to attempt to maintain a sharp liquid-gas interface and minimize numerical diffusion. One observes in Figure 3, that the applied acceleration, to the right, causes the liquid phase (outer phase) to be compressed against the left-hand wall, causing the flow to push the helium gas bubble to the right. This motion is modeled by both the NMM and CFD models.

The tank slosh scenario is modeled as a closed domain with the origin at the center of the tank, with a single no-slip wall boundary condition expressed as

$$\mathbf{u} = \mathbf{0}, \qquad \nabla p\cdot\hat{\mathbf{n}} = 0, \qquad \nabla\alpha\cdot\hat{\mathbf{n}} = 0. \tag{21}$$

The tank is considered to be initially quiescent ($\mathbf{u}(x,0) = \mathbf{0}$) at a uniform temperature of eighty Kelvin and pressure of one atmosphere. The gas phase is assumed to initially be collected into a spherical bubble in the center of the tank, with radius R_{gas}. The initial volume phase fraction field is initialized as

$$\alpha(x,0) = \begin{cases} 0 & r = \sqrt{x^2+y^2+z^2} < R_{gas} \\ 1 & \text{otherwise} \end{cases} \tag{22}$$

The tank sloshing is driven by an applied acceleration, which is the modeled result of one of the spacecraft's thrusters firing and causing the spacecraft to briefly accelerate in a particular direction. For a typical hypergolic thruster applied to a tank of the prescribed size and fluid fill, the acceleration will be in the range of $0.01 - 0.1$ m/s^2 and will have a subsecond duration. For this study, we choose a duration of 0.05 s. The acceleration is applied along one of the minor axes of the cylindrical tank over the entire volume.

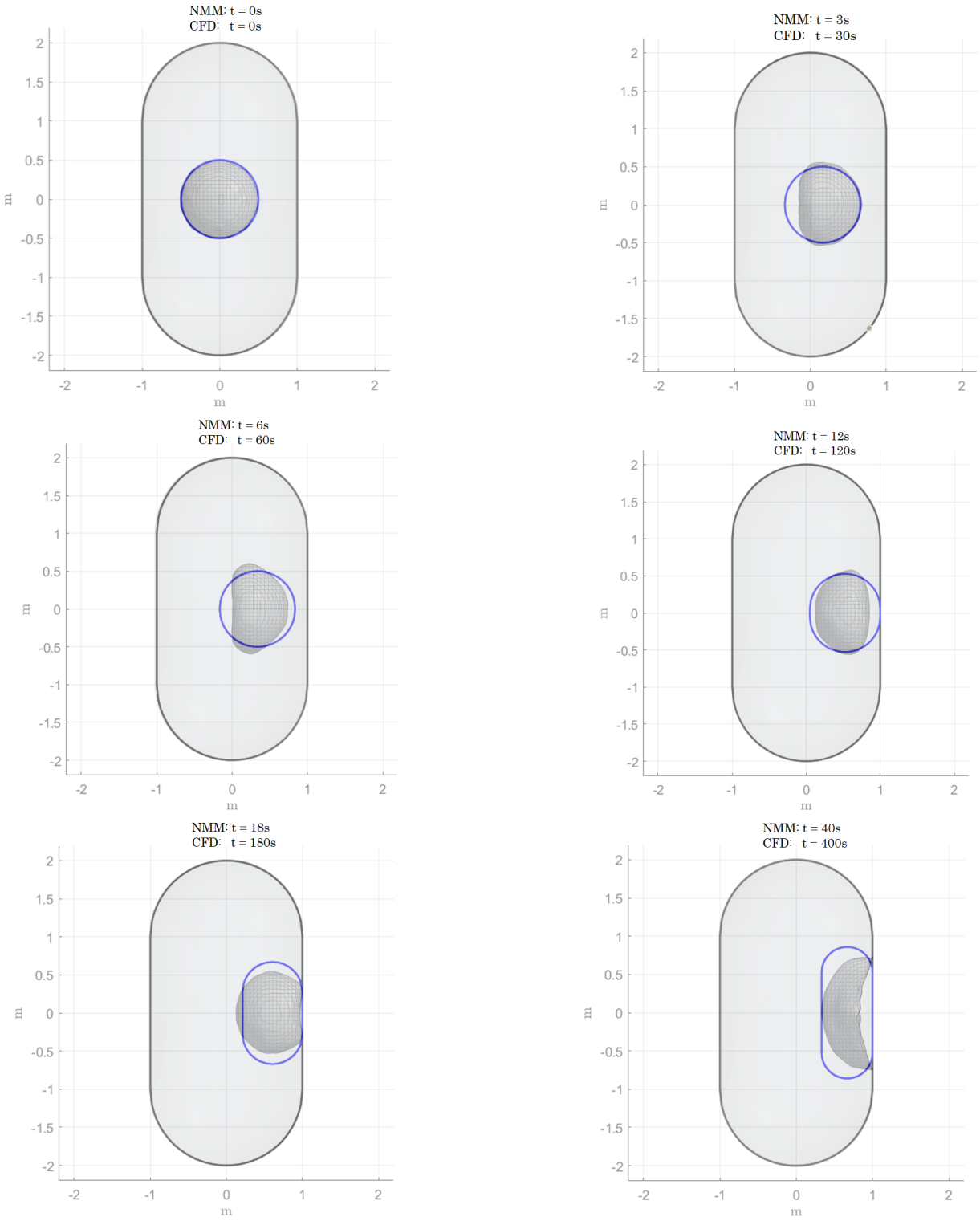

Fig. 3 The liquid-gas interface at different time intervals.

Figure 3 shows the position of the free surface interface between the liquid oxygen and helium gas phases at several times, for the case of $a = 0.1$ m/s^2. One observes that the applied acceleration, to the left, causes the liquid phase (outer phase) to be compressed against the left hand wall, causing the flow to push the helium gas bubble to the right. After

roughly 400 seconds, the bubble is positioned against the right wall and did not have an appreciable change of shape or position through a run of 2000 seconds. This is observed in the center of mass as well, as after the bubble becomes attached to the wall, it stays in such a configuration and does not detach through 2000 seconds.

IV. Negative Mass Model Simulation

The NMM simulation integrates the dynamics of the bubble with respect to time, which moves in the opposite direction of the fluid. The density of the fluid is assumed to be uniform and incompressible, and by extension, the bubble, likewise, has a constant volume. The density of the bubble is assumed to be negligible when compared with the density of the liquid oxygen (0.166 kg/m^3 compared to 1141 kg/m^3).

In Figure 3, an initial perturbation causes the fluid or, more specifically, the air bubble to move. The initial perturbing forces during this simulation are modeled as a 6-element acceleration vector $a \in \mathbb{R}^6$, and the centroid of the mass is tracked relative to the geometric center of the mass of the tank.

The inertia of the shapes predicted by the model are well understood, which enables the estimation of the inertia of the fluid by looking at the difference between the inertia of a full tank when compared to the inertia of the negative mass bubble. Ongoing work seeks to demonstrate the validity of this estimation method.

V. Results

The results of this work are presented in three case studies, each exploring a different aspect of the dynamics. The first case study was first introduced in Figure 3 and considered a high fill ratio and a simple horizontal perturbation for simplicity. The second case study seeks to explore low fill ratio scenarios and uses the case of main engine cutoff (MECO) of a Falcon 9 rocket to demonstrate the model's performance even when a low amount of fluid is present. The third and final case study again considers a high fill ratio, but the perturbation is caused by a single thruster oriented to produce rotational motion on the tank as well as translational motion, resulting in force about 5 out of 6 axes.

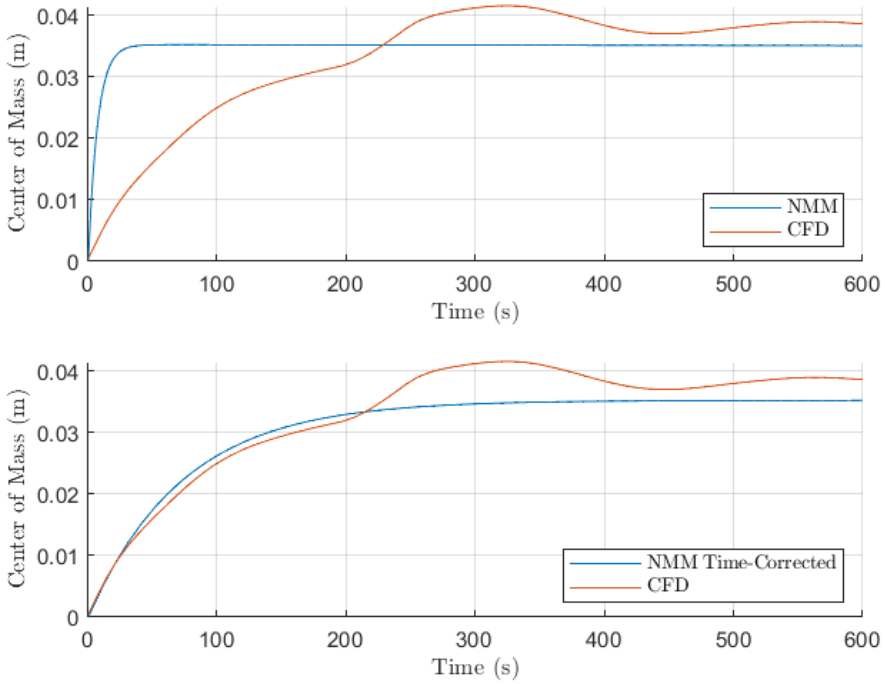

Fig. 4 The center of mass along the x-axis of the NMM compared to the CFD simulation. The bottom plot shows the time-corrected displacement illustrated in Figure 3.

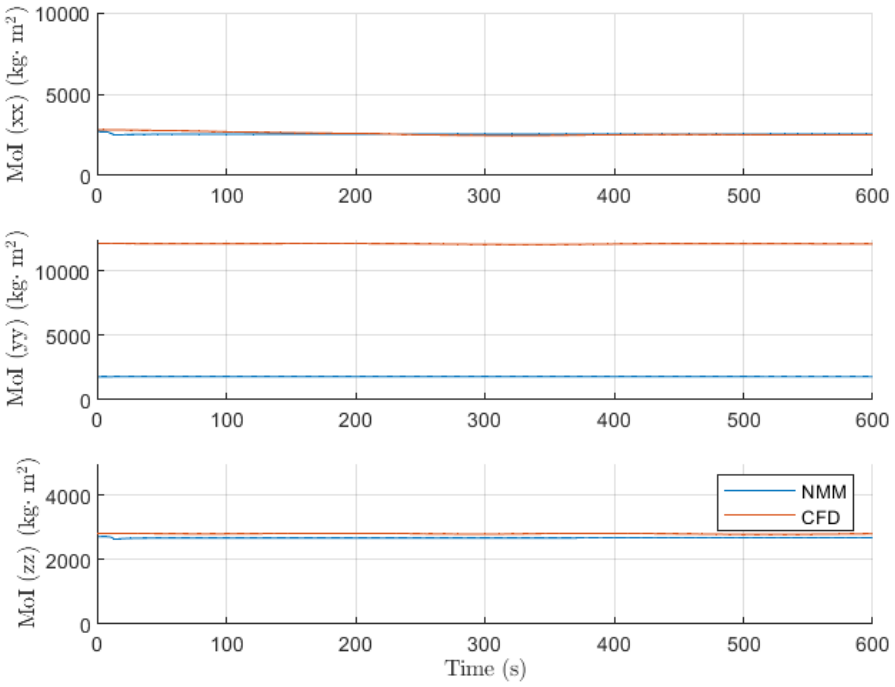

Fig. 5 The diagonal moments of inertia estimated by the NMM as compared to the CFD simulation.

A. Case Study: Horizontal Perturbation with High Fill Ratio

The first case study compares the performance of the NMM and CFD models for a simpler horizontal perturbation at 0.1 m/s^2. The bubble is initialized as a sphere at the center of the tank with a radius of 0.5 m. In all cases, the tank dimensions are pill-shaped with a radius of 1 m and a height of 4 m, making the cylindrical portion 2 m tall with spherical hemispheres on each end. This case study is illustrated in Figure 3, and the results of the center of mass for both the CFD and NMM cases are shown in Figure 4. Diagonal moments of inertia were also estimated using the moments of inertia of a solid capsule augmented by the findings of [10], which multiplied the axial moment by 0.19 and the perpendicular moments by 0.17 when considering liquid moments instead of solid ones. Then, the off-axial moment of the air bubble was subtracted from the total. The results are shown in Figure 5, with good convergence on the perpendicular moments but very poor convergence with the axial moment. The cause of this discrepancy between the NMM estimate and the integrated density over volume in the CFD simulation is still being investigated and persists in all case studies.

B. Case Study: MECO with Low Fill Ratio

Next, a low fill ratio case is explored during main engine cut-off (MECO) of a Falcon 9 launch vehicle, based on a video provided by SpaceX of the behavior of liquid oxygen inside the tank [11]. In this case study, the fluid rapidly goes from 5 g's to microgravity and begins to slosh gently. In the simulation, the small perpendicular perturbations are not known, only the axial change in acceleration. CFD simulations show that the sloshing fluid sticks to the side of the tank but oscillates between hemispheres after shutdown, demonstrating more excited behavior than is visible in the video.

C. Case Study: Spacecraft Maneuver with High Fill Ratio

Finally, a full rigid body simulation of a refueler logistics module is explored. For this case study, refer to Table 2 where R_2 and R_3 are rotation matrices about the second and third principal axes, respectively. A burn time of 1 second is performed by a single thruster with a constant thrust of 300 N. As with previous scenarios, the center of mass tracks the same trend as the CFD model, but at a much faster time scale.

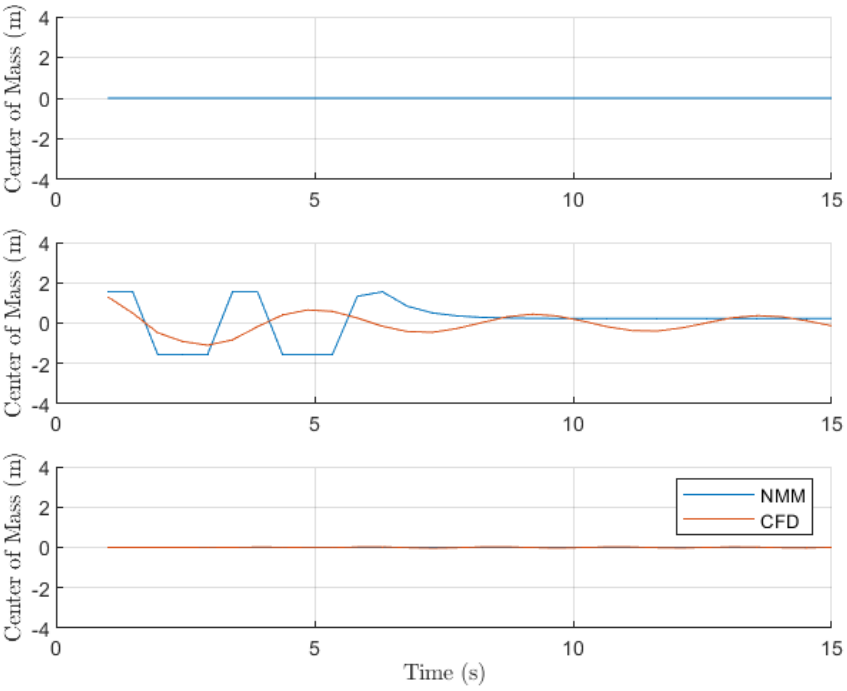

Fig. 6 The center of mass along the all axes of the NMM compared to the CFD simulation during MECO that goes from 5 to 0 g's.

Table 2 Spacecraft properties used in the third case study

Property	Value
Motor Position	${}^{\mathcal{B}}r_{\mathcal{M}} = [-1, 0.5, 0.5]^T$ m
Motor Attitude	${}^{\mathcal{B}}R_{\mathcal{M}} = R_2(\frac{\pi}{6})R_3(\frac{5\pi}{6})$ rad
Motor Thrust	$T_{\mathcal{M}} = 300$ N
Burn Time	$t_b = 1$ s
Spacecraft Dry Mass	$m_{sc} = 2500$ kg
Fluid Mass	$m = 18520$ kg
Control input	$u = [0, 0, 0, 0, 0, -T_{\mathcal{M}}]^T$

VI. Conclusion

This work has introduced an expansion on the spring-mass-damper model for sloshing cryogenic fluid in a microgravity environment using physical constraints for the boundary of an arbitrarily sized tank. This model, known as the negative mass model (NMM), tracks the bubble instead of the fluid and, using geometry approximations of bubble size and knowledge of tank geometry, can accurately predict the steady-state convergence of the center of mass of the tank. The NMM also overestimates the rate of displacement of the bubble by a factor of 10, but NMM can accurately predict CFD bubble dynamics by adjusting for this.

The method described herein also shows promise in the estimation of moments of inertia of sloshing fluids. Perpendicular moments of inertia are able to converge rapidly, though significant error exists in axial moments of inertia estimates. However, in the first case study, the NMM can converge on these estimates in less than a second, whereas the CFD simulation running on a comparable machine takes several hours to perform the same simulation. Thus, the trade-off between accuracy and computational load is such that the NMM remains useful, even in this early stage.

Future work seeks to improve the simulation by including higher fidelity coefficients that better track the motion of

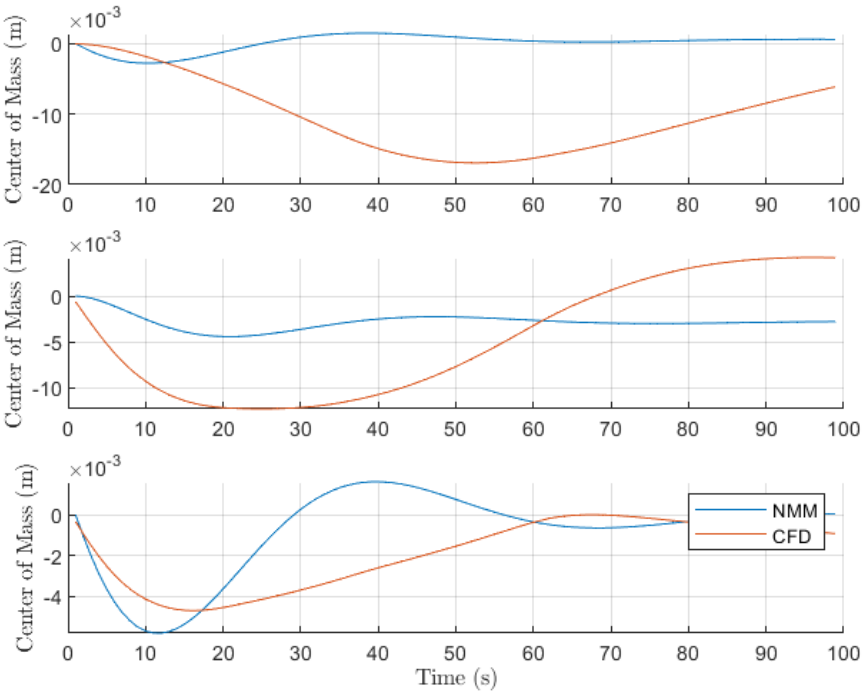

Fig. 7 The center of mass along all axes of the NMM compared to the CFD simulation for the coupled motion simulation. Note the scale of the y-axis.

the bubble. Furthermore, a more accurate model for axial moments of inertia of a fluid is desired, as there remains a significant difference between the CFD estimate and the estimate from the NMM. Next, determining a way of slowing down the motion predicted by the NMM to one-tenth of the current speed to better match CFD predictions would be desirable, while still preserving the connection to physical fluid characteristics. Finally, understanding the difference between the dampening caused by viscosity and the experimentally derived value of $\frac{\gamma}{m} = 0.87\ \mathrm{s}^{-1}$ is necessary before this model is implemented practically.

References

[1] Bolton, S., Lunine, J., Stevenson, D., et al., "The Juno Mission," *Space Sci Rev 213*, Vol. 5, No. 37, 2017. https://doi.org/10.1007/s11214-017-0429-6.

[2] Vreeburg, J., "Dynamics and control of a spacecraft with a moving pulsating ball in a spherical cavity," *Acta Astronautica*, Vol. 40, No. 2, 1997, pp. 257–274. https://doi.org/https://doi.org/10.1016/S0094-5765(97)00095-7, enlarging The Scope of Space Applications.

[3] Hung, R., and Pan, H., "Mathematical model of bubble sloshing dynamics for cryogenic liquid helium in orbital spacecraft dewar container," *Applied Mathematical Modelling*, Vol. 19, No. 8, 1995, pp. 483–498. https://doi.org/https://doi.org/10.1016/0307-904X(95)00033-G.

[4] Saltari, F., Traini, A., Gambioli, F., and Mastroddi, F., "A linearized reduced-order model approach for sloshing to be used for aerospace design," *Aerospace Science and Technology*, Vol. 108, 2021, p. 106369. https://doi.org/https://doi.org/10.1016/j.ast.2020.106369.

[5] Marsell, B., Gangadharan, S., Chatman, Y., Sudermann, J., Schlee, K., and Ristow, J., *A CFD Approach to Modeling Spacecraft Fuel Slosh*, 2009. https://doi.org/10.2514/6.2009-366, URL https://arc.aiaa.org/doi/abs/10.2514/6.2009-366.

[6] Wittal, M. M., Asher, B. W., McCann, B. S., and Nazari, M., "Autonomous Control for Arbitrary Thruster Configurations and Mass Properties in Special Euclidean Group SE(3)," *74th International Astronautical Congress*, , No. IAC-23,C1,3,2,x78246, 2024.

[7] Lemmon, E. W., Bell, I. H., Huber, M. L., and McLinden, M. O., *Thermophysical Properties of Fluid Systems*, National Institute of Standards and Technology, 2024, Chaps. NIST Chemistry WebBook, NIST Standard Reference Database.

[8] Brackbill, J. U., Kothe, D., and Zemach, C., "A Continuum method for modeling surface tension," *J. Comp. Physics*, Vol. 100, 1992, pp. 335–354.

[9] Jurns, J. M., and Hartwig, J. W., "Liquid oxygen liquid acquisition device bubble point tests with high pressure lox at elevated temperatures," *Cryogenics*, Vol. 52, 2012, pp. 283–289.

[10] Dodge, F., and Kana, D., "Moment of Inertia and Damping of Liquids in Baffled Cylindrical Tanks," *NASA Contractor Report*, Vol. NASA CR-383, No. NAS 8-1555, 1966.

[11] SpaceX, "SpaceX CRS-4 Launch - Fuel Slosh, internal fuel tank camera (5G to 0G)," https://youtu.be/u656se4e34M?t=67, 2015. [Online; accessed 24-January-2024].